Improvement of the perovskite photodiodes performance via advanced interface engineering with polymer dielectric

A.P. Morozov, L.O. Luchnikov, S. Yu. Yurchuk, A.R. Ishteev, P.A. Gostishchev, S.I. Didenko, N.S. Saratovsky, D.O. Balakirev, I.V. Dyadishchev, A.A. Romanov, E.A. Ilicheva, A.A. Vasilev, S.S. Kozlov, D.S. Muratov*, Yu. N. Luponosov* and D.S. Saranin*

Cite this article as: A.P. Morozov, *et.al*. Improvement of the perovskite photodiodes performance via advanced interface engineering with polymer dielectric. *Light: Advanced Manufacturing* accepted article preview 24 February 2025; doi: 10.37188/lam.2025.024

Received 15 July 2024; Revised 13 February 2025; Accepted 18 February 2025; Accepted article preview online 24 February 2025

Improvement of the perovskite photodiodes performance via advanced interface engineering with polymer dielectric

A.P. Morozov[1§], L.O. Luchnikov[1§], S. Yu. Yurchuk[2], A.R. Ishteev[1], P.A. Gostishchev[1], S.I. Didenko[2], N.S. Saratovsky[3], D.O. Balakirev[3], I.V. Dyadishchev[3], A.A. Romanov[2], E.A. Ilicheva[1], A.A. Vasilev[2], S.S. Kozlov[4], D.S. Muratov[5*], Yu. N. Luponosov[3*] and D.S. Saranin[1*]

[1]LASE – Laboratory of Advanced Solar Energy, NUST MISiS, 119049 Moscow, Russia
[2]Department of semiconductor electronics and device physics, NUST MISiS, 119049 Moscow, Russia
[3]Enikolopov Institute of Synthetic Polymeric Materials of the Russian Academy of Sciences (ISPM RAS), Profsoyuznaya St. 70, Moscow, 117393, Russia

[4]Laboratory of Solar Photoconverters, Emanuel Institute of Biochemical Physics, Russian Academy of Sciences, 119334 Moscow, Russia

[5]Department of Chemistry, University of Turin, 10125, Turin, Italy

§: The authors contributed equally to this work

Corresponding authors: Dr. Danila S. Saranin saranin.ds@misis.ru, Dr. Dmitry S. Muratov dmitry.muratov@unito.it, Dr. habil. Yu. N. Luponosov luponosov@ispm.ru

Abstract

Halide perovskite-based photodiodes are promising for efficient detection across a broad spectral range. Perovskite absorber thin-films have a microcrystalline morphology, characterized by a high density of surface states and defects at inter-grain interfaces. In this work, we used dielectric/ferroelectric poly(vinylidene-fluoride-trifluoroethylene) (P(VDF-TrFE)) to modify the bulk interfaces and electron transport junction in p-i-n perovskite photodiodes. Our complex work demonstrates that interface engineering with P(VDF-TrFE) induces significant Fermi level pinning, reducing from 4.85 eV for intrinsic perovskite to 4.28 eV for the configuration with dielectric interlayers. Modifying the interfaces in the devices resulted in an increase in the key characteristics of photodiodes compared to pristine devices. The integration of P(VDF-TrFE) into the perovskite film didn't affect the morphology and crystal structure, but significantly changed the charge transport and device performance. IV curve analysis and 2-diode model calculations showed enhanced shunt properties, a decreased non-ideality factor, and reduced saturation dark current. We have shown that the complex introduction of P(VDF-TrFE) into the absorber's bulk and on its surface is essential to reduce the impact of the trapping processes. For P(VDF-TrFE) containing devices, we increased the specific detectivity from 10^{11} to ~10^{12} Jones, expanded the linear dynamic range up to 100 dB, and reduced the equivalent noise power to 10^{-13} W·Hz$^{-1/2}$. Reducing non-radiative recombination contributions significantly enhanced device performance, improving rise/fall times from 6.3/10.9 µs to 4.6/6.5 µs, and achieved photo-response dynamics competitive with state-of-the-art analogs. The cut-off frequency (3dB) increased from 64.8 kHz to 74.8 kHz following the introduction of the dielectric. We also demonstrated long-term stabilization of PPD performance under heat-stress. These results provide new insights into the use of organic dielectrics and an improved understanding of trap-states/ion defect compensation for detectors based on perovskite heterostructures.

KEYWORDS: perovskite photodiodes, dielectrics, heterostructures

Halide perovskite (**HPs**) based photodiodes (**PD**s) have emerged as a promising technology in the field of thin-film optoelectronics for a wide array of applications, including medical imaging[1], high-resolution sensing[2], and optical communication[2]. Perovskite refers to a class of materials with the general chemical formula ABX_3[3], where the A-cation is an organic cation ($CH(NH_2)_2^+$ - FA^+) or inorganic cesium (Cs^+); the B-cation is typically lead (Pb^{2+}), and the X-anion is iodine (I), bromine (Br^-), or chlorine (Cl^-). These materials exhibit unique combination of semiconductor properties for efficient photoelectric conversion, including strong optical absorption (>10^4 cm^{-1})[4,5], reasonably high charge-carrier mobility[6] and wide range of band-gap tunability (from 1.2 to 2.8 eV)[7,8]. Typically, HP-based photodetectors are thin-film devices with a microcrystalline absorber, sandwiched between charge-transporting layers of p-type and n-type materials. The use of p-i-n oriented HP based PDs allows to reach competitive output performance with detectivities in the range 10^{12}-10^{13} Jones[9,10] which a comparable with benchmarks in the industry of sensors like amorphous Si. The utilization of various solution-processing techniques (slot-die[11], ink-jet printing[12]) offers opportunities for low-cost industrial fabrication[13]. HP devices were considered 'defect-tolerant' materials[14] due to their reduced dynamics of non-radiative recombination processes[15]. However, various reports estimating the numerical parameters of trap states[16–18] highlight the presence of deep states with concentrations up to 10^{14} cm^{-3}. Structural imperfections, point defects, and impurities, typically associated with grain boundaries and interfaces in HP devices, can significantly affect device performance. The migration of ionic defects can lead to several detrimental effects, including hysteresis[19], charge accumulation[20], increased leakage current[21], longer rise times, and signal decay. Additionally, clusters of charged defects or decomposition products of the perovskite molecule can initiate electrochemical corrosion at interfaces[22], associated with oxidation processes. Researchers have attempted to mitigate these challenges with various materials for inter-grain passivation[23]. The parasitic trapping processes in HP photodetectors could occur in the perovskite (bulk recombination) and at the charge collection junction with p- and n-type transporting layers (surface recombination), respectively [24,25]. Most efforts to passivate surfaces in HP photodiodes (PPDs) focus on modifying a single interface[26–28].

The study conducted by *Ollearo et al.* revealed that modifying the hole transport interface with polymer thin-films yielded improvements in energy level alignment, leading to a decrease in dark current to 10^{-11} A/cm2 and noise equivalent power to 2 × 10−14 A $Hz^{-1/2}$. *Wonsum Kim* and *colleagues*[29] passivated grain boundaries by adding a PMMA interlayer between the perovskite and ETL. This method has decreased the noise equivalent power (NEP) from 2520 $fW/Hz^{1/2}$ to 230 $fW/Hz^{1/2}$, but the response speed and cutoff bandwidth were also reduced. Improving device performance requires a more comprehensive approach. Forming heterostructures with wide-gap semiconductors and dielectrics is an effective strategy to enhance the performance of photodetectors (PDs). The presence of ultrathin dielectric layers at the interface can facilitate better charge extraction by modifying the electric field distribution within the photodiode[30]. Generally, the key advantages include improved carrier confinement, reduced band-bending, decreased

interface trap-states density, and high-frequency capabilities. Notably, the effectiveness of semiconductor-ultrathin dielectric interfaces has been demonstrated in various configurations: high-K materials for GaAs devices (Hf-based)[31,32], conventional dielectrics (Al_2O_3, Si_3N_4)[32], and insulating polymers (polyimide)[33]. Perovskite photodiodes face a greater challenge in addressing this issue. It involves passivating the intergranular boundaries of the microcrystalline absorber and surface with selective transport layers that are prone to iodine-containing defects diffusion[34]. Among various polymer dielectric materials, which can be used for the passivation of perovskite-based devices the most interesting those based on polyvinylidene fluoride (PVDF), due to its unique ferroelectric and dielectric properties [35]. In general, ferroelectric materials can be polarized and generate a built-in electric field to separate the photogenerated electron-hole pairs. However, due to the high crystallinity and insufficient solubility of PVDF, its copolymers, especially those with trifluoroethylene, have become more widely used because their thin and uniform films can be easily obtained by standard solution methods[36–38]. Several groups have already described integration of poly(vinylidenefluoride-trifluoroethylene) (P(VDF-TrFE) into the perovskite absorber layer to manipulate the carrier transfer behavior of the devices[39,40]. Typically, research on the integration of dielectrics into photodiode structures considers only one type of application, either modifying the inter-grain interfaces in the absorber or at the contact with charge-transport layers. However, integrated interface modification using single P(VDF-TrFE) films for compensation of charged species in both cases may provide a synergistic effect. On the one hand, this impacts the generation and recombination processes, while on the other hand, it affects the extraction and transport of photocarriers. The combinational impact of the dielectrics application in perovskite photodiodes remains sufficiently unexplored and requires deep investigation.

State-of-the-art passivation materials for perovskite diode devices[41,42], including photodiodes and solar cells, often involve organic dielectrics such as polymethyl methacrylate[43] and polyethylene glycol[44]. Polymer integration into solution processing typically focuses on interface modification or matrix formation to control nucleation and crystallization. Promising results have also been reported with fluorine (F) - containing materials[45]. The literature highlights the effective use of F-containing additives (inorganic fluoride salts, fluorinated organic small molecular materials, ionic liquids), which form hydrogen bonds with organic and Pb-cations in perovskite molecules[46]. As reported[46–48], this compensates surface states and enhances the resistance of perovskites to degradation induced by hydrolysis. Poly (vinylidene fluoride) (PVDF) polymers offer the advantages of chain templating and passivation due to the F-atoms in the composition. Modification of photodiode interfaces presents unique challenges, requiring strong shunt properties, efficient photocarrier transport across a wide range of light intensities, and fast response times. In this context, studying the properties of PVDF-modified PPDs across different modes of operation is an important task for in-depth analysis. The PVDF-TrFE copolymer exhibits a higher atomic fraction of fluorine and enhanced solubility in the solvents utilized for the fabrication of perovskite-based layers in comparison to PVDF. In this regard, this renders it a more promising candidate for industrial applications.

In this paper, we present a comprehensive study on the modification of the perovskite absorber and the n-type collection interface using a promising organic polymer dielectric/ferroelectric P(VDF-TrFE). In this work, we reveal the effects of P(VDF-TrFE) integration on the optoelectronic and surface properties of multicationic perovskite thin films and investigate the reasons for changes in charge carrier transport in p-i-n diode structures. For the first time, we demonstrate that the complex implementation of ultrathin dielectric layers improves the wide spectra of the photo-response parameters (specific detectivity, noise equivalent power, linear dynamic range, signal-to-noise ratio), but also increases the fast response and cut-off frequency without special pre-conditioning. The obtained results are thoroughly analyzed and discussed.

Results and discussions

In this research, we developed a novel modification of the microcrystalline perovskite absorber ($Cs_{0.2}FA_{0.8}PbI_{2.93}Cl_{0.07}$) interfaces by utilizing P(VDF – TrFe). The copolymers of this material possess a combination of low dielectric constants with relatively high glass transition temperature, transparency, structural flexibility, ease of solution processing, and chemical stability [49]. We employed ultrathin P(VDF-TrFE) dielectric interlayers at the grain boundaries within the perovskite film and at the absorber/electron transport layer interface. The schematics of HP based photodiodes (**PDs**) developed in this work and molecular structure of P(VDF-TrFE) presented in the **fig.1**.

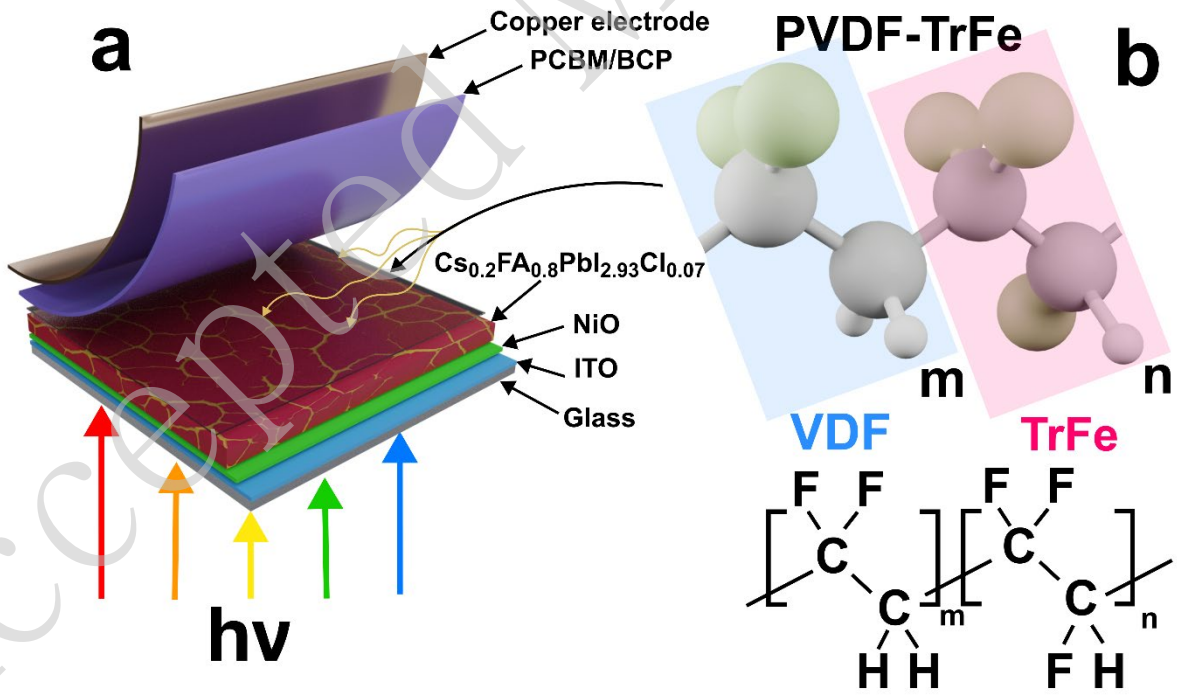

Figure 1 – Photodiode scheme (a) with P(VDF-TrFE) structure visualization and formula (b)

The devices were fabricated with a p-i-n architecture: glass (1.1 mm)/ITO (anode, 330 nm)/NiO (p-type, 30 nm)/perovskite absorber $Cs_{0.2}FA_{0.8}PbI_{2.93}Cl_{0.07}$ (450 nm)/PCBM (n-type, 30 nm)/BCP (hole

blocking interlayer, 10 nm)/Copper (cathode, 100 nm). The solubility of P(VDF-TrFE) in solvents like dimethylformamide and N-methyl pyrrolidone allowed its integration into the perovskite solution for subsequent deposition and crystallization. Through this technological approach, we achieved a bulk distribution of the dielectric within the microcrystalline absorber. P(VDF-TrFE) deposition on the back surface of $Cs_{0.2}FA_{0.8}PbI_{2.93}Cl_{0.07}$, was also carried out by solution-processing. A detailed description of the experimental section presented in the Electronic Supplement Information file (**ESI**). Fabrication of the different types of samples was associated with modifying the perovskite absorber interfaces. To simplify the titles of the different configurations, we designated the bare perovskite films as "control". The sample with an P(VDF-TrFE) distributed into the bulk of $Cs_{0.2}FA_{0.8}PbI_{2.93}Cl_{0.07}$ was designated as "Bulk", and the sample with dielectric incorporated to the bulk and electron collection junction was referred as "Bulk/n-side".

We examined the optical properties of perovskite layers with dielectric interlayers using Tauc plots and photoluminescence spectra (**fig.S1** in **ESI**). The calculation was realized using equations **S1** (**ESI**). The analysis of absorption properties analyses for thin-films demonstrated edge shifts (**fig.S1(a), ESI**). The band-gap energy (E_g) was extracted using linear approximation, revealing that the E_g of the control sample was 1.573 eV. Integrating dielectric interlayers led to a decrease of the E_g. The band-gap value for Bulk sample was 1.571 eV, while for Bulk/n-side the E_g reduced to 1.570 eV. The analysis of peak positions in the photoluminescence spectra (**fig.S1(b), ESI**) correlated with the absorption data. Thin films containing dielectric interlayers exhibited a 'red shift.' The peak positions were 1.592 eV (779 nm) for the control, 1.583 eV (783 nm) for Bulk, and 1.581 eV (784 nm) for Bulk/n-side.

The influence of P(VDF-TrFE) on perovskite films' morphology and phase composition was investigated through AFM (**Fig.2(a-c)**) and XRD (**Fig.2d**). Analysis revealed that bare perovskite absorber and P(VDF-TrFE) containing samples predominantly exhibited the β-$Cs_{0.2}FA_{0.8}PbI_{2.93}Cl_{0.07}$ phase, characterized by specific peaks at 20.6º, 29.3º, 36.14º, 41.9º, and 47.15º. Furthermore, distinct peaks corresponding to the ITO substrate were observed, along with peaks signifying lead iodide at 18.5° (001) and 39.2° (101). No signs of peak shifting or broadening were detected. So, integration of the P(VDF-TrFE) hadn't discernible quantitative or qualitative effect on the phase composition of the perovskite layer. To examine the impact of polymers on the optoelectronic properties of perovskite, KPFM measurements were conducted using an NT-MDT Ntegra AFM equipped with a NSG03/Au tip. The work function (W_f, **Fig. 2e**) was determined with a fresh HOPG surface serving as the energy baseline (see details of the calculations in the **eq.S2,S3** in **ESI**). The Fermi energy of the control sample is 4.85 eV. Incorporating PVDF into the perovskite volume shifts the Fermi level to 4.16 eV. Applying PVDF to the bulk sample increased the work function from 4.16 eV to 4.28 eV. Both bulk and bulk/n-side samples displayed a significant decrease in work function, up to 0.7 eV for the bulk sample, compared to the control perovskite film.

The incorporation of P(VDF-TrFE) into the bulk and at the interfaces of perovskite can induce the reconfiguration of the trap states. P(VDF-TrFE), a ferroelectric polymer, has been shown to influence the electronic properties of perovskite materials[50] by reconfiguring intrinsic defects and trap states, leading to

improved charge separation and reduced recombination. The shift in work function from 4.85 eV (intrinsic conditions) to 4.28 eV for the Bulk/n-side sample indicates an alignment favorable for electron transport, which could be attributed to the modification of trap states at the interface and within the bulk of the perovskite. The observed Fermi level pinning (FLP) [51–53] effect may be caused by the ferroelectric properties of P(VDF-TrFE), potentially through the compensation of charged states[54]. The enhancement of local fields and the formation of dipoles at intergranular boundaries can screen or compensate for states induced by ionic defects, whose concentration in $Cs_{0.2}FA_{0.8}PbI_{2.93}Cl_{0.07}$ thin-films can reach up to 10^{14} cm^{-3}[55]. The work-function of thin-films based on hybrid perovskites is highly sensitive to the influence of defects and doping additives. Even small concentrations of nanomaterials introduced during solution processing can alter the work function by ~0.1 eV. In our previous work on modifying perovskite absorbers with functionalized titanium carbides (Ti_3C_2)[56,57], we found that solution-processed nanomaterials at a concentration of 10^{-2} mg/mL could shift the perovskite energy levels by approximately 0.4 eV, mainly due to the influence of terminal groups (O^-, Cl^-, F^-)[58].

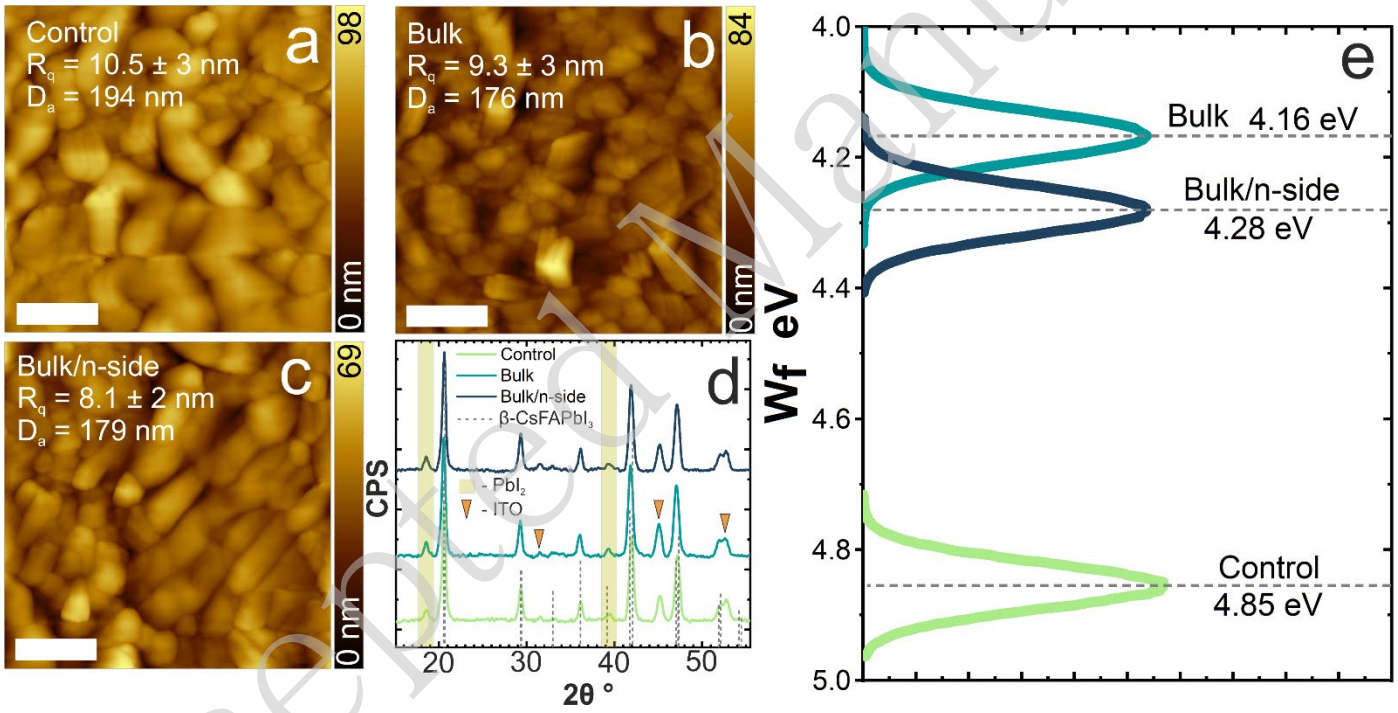

Figure 2 – morphology (a-c), X-Ray diffraction (d) and surface work function of perovskite films (e); sale bar 500 nm

To evaluate the recombination dynamics in thin films with dielectric interlayers, we used high time-resolved luminescence (TRPL) measurements (**fig.S2** in **ESI** and **tab.1**). Photo-carrier lifetime values were extracted by fitting eq.: $I(t)=A_1\exp(-x/\tau_1)+A_2\exp(-x/\tau_2)$ (double exponent fit). For relevant data, we collected batch statistics from at least six samples for the control, bulk, and bulk/n-side samples. The median lifetime (τ) of the control $CsFAPbI_3$ was 72.6 ns. The integration of P(VDF-TrFE) into the intergranular boundaries minimally changed τ to 74.6 ns. For the Bulk/n-side configuration, a more substantial increase in τ to 82.6 ns (+14% compared to the control) was observed. Interpreting TRPL data is a complex task. For

the fast component, the τ_1 value decreased from 8.9 ns to 6.9 ns with P(VDF-TrFE) integration, potentially indicating a reduced contribution of trap-assisted recombination [59,60]. For the slow component, τ_2, which may be influenced by exciton states[61,62], we observed inverse correlations. We assume that this trend could result from the local polarization of P(VDF-TrFe) during the photo-injection of electron-hole pairs and the resulting accumulation effects in the enhanced electric field.

Table 1 - TRPL normalized data for perovskite films NiO/Control; NiO/Bulk; NiO/Bulk/n-side

Sample configuration		A_1, ÷10^3	τ_1 (ns)	A_2, ÷10^3	τ_2 (ns)	$\tau_{average}$ (ns)
Control	median	6.9	8.9	20.7	75.1	72.6
	average	7.2	8.6	21.0	77.4	74.9
	± std	± 0.8	± 1.1	± 4.3	± 14.8	± 14.7
Bulk	median	6.3	8.1	21.6	76.6	74.6
	average	6.3	8.2	21.2	76.6	74.5
	± std	± 0.6	± 0.8	± 1.4	± 2.4	± 2.1
Bulk/n-side	median	7.9	6.9	20.3	81.6	79.2
	average	7.8	6.9	20.5	85.0	82.6
	± std	± 0.7	± 0.4	± 1.3	± 8.2	± 8.0

Notes: A_1 and A_2 is intensity amplitudes; τ_1 and τ_2 is luminescence lifetimes; $\tau_{average}$ is a weighted average luminescence lifetime; std is standard deviation.

To investigate the impact of the interface modification on diode properties, we measured the dark volt-ampere characteristics (JVs) for the fabricated PPDs with bias range from -0.1 V to +1.1 V, as shown in **Fig.3**. The dark JV curves of the fabricated photodiodes exhibited typical diode behavior, characterized by relevant rectification. Generally, the dark JV curve can be divided into four main regions related to the shunt current (I), recombination current (II), diffusion current (III), and contact resistance (IV). We observed that integrating the dielectric both within the bulk and at the n-type interface altered the diode properties, indicating notable changes in the charge carrier transport. The minimum value of the dark current density (J_{min}) measured at zero bias was $1x10^{-7}$ A/cm^2 for the reference device. In contrast, the values for the Bulk and Bulk/n-side configurations were significantly reduced by an order of magnitude, up to $2x10^{-8}$ A/cm² and $7x10^{-10}$ A/cm², respectively. The use of P(VDF-TrFE) further contributed to reducing the dark leakage current ($J_{leakage}$, bias= -0.1 V). The control and bulk PPDs exhibited comparable $J_{leakage}$ values ~$2x10^{-6}$ A/cm^2, whereas the bulk/n-side configuration demonstrated a significant reduction to 9.7×10^{-8} A/cm². The box—charts for data of J_{min} for PPDs presented in the **fig. S3 (ESI)**, which represents clear correlation between J_{min} value and integration of P(VDF-TrFE). Calculating the shunt resistance (R_{sh}) values showed an increase for devices with integrated dielectrics at the interfaces. The reference device had an R_{sh}=4.2 kOhm·cm², which increased to 6.8 kOhm·cm² for the bulk configuration and reached 1.2 MOhm·cm² for the Bulk/n-side device. P(VDF-TrFE) was used to modify the perovskite layer interfaces at low solution concentrations (~10^{-3} mg/mL). Relatively low concentration was selected to avoid the negative impact that higher P(VDF-TrFE) concentrations had on the diode properties of the devices (**fig. S4**, **ESI**). The increase

of the concentration to 10^{-1} mg/mL resulted in decrease of R_{sh} from ~10^{1} Ohm·cm^2 (P(VDF-TrFE) concentration 10^{-3} mg/mL) to ~10^{3} Ohm·cm^2.

For a comprehensive analysis of the changes in the dark JV curve in the II and III regions, we performed a fitting using a 2-diode model to extract the appropriate parameters (**tab.2** with values of the non-ideality factors (m_1, m_2); reverse saturation currents (J_{01}, J_{02}), and shunt resistance).

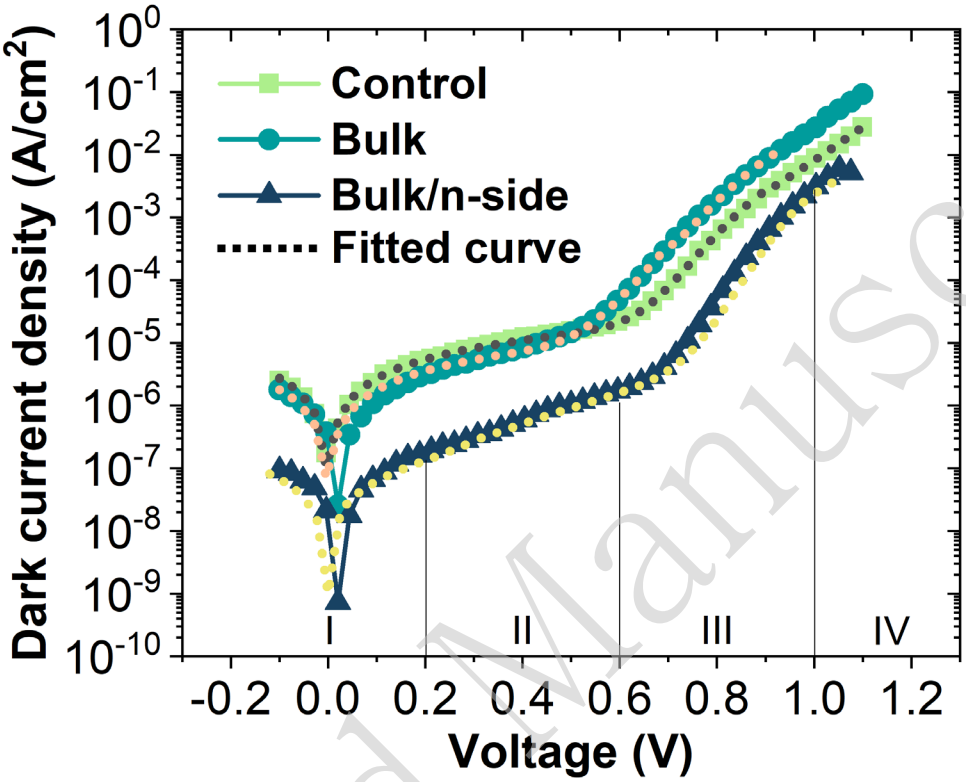

Figure 3 – Dark JV curves of p-i-n structures of the PPDs with dielectric interlayers

Generally, the total saturation dark current (J_0) is governed by recombination processes within the solar cell and can be utilized to estimate the efficiency of charge carrier transport. In hetero-structured devices, J_0 depends on the number and quality of interfaces. In our study, we modified the interfaces within the perovskite absorber volume and at the junction for electron collection. Calculations for dark JV were performed according to the equations **S4-S11** (**ESI**), the equivalent circuit of the 2-diode model presented in **ESI** (**fig.S5, ESI**). The calculated values of J_0 indicated that the overall value is primarily determined by J_{02}. The significant reduction of J_0 from 10^{-4} to 10^{-8} A/cm² in devices with P(VDF-TrFE) integration compared to control highlights the reduced contribution of recombination to charge carrier transport. The non-ideality factor of a photodiode is typically used to analyze the dominant recombination mechanisms involving free carriers and traps both in the volume (bulk) and at interfaces. Interpreting the calculated values of the non-ideality factor for photovoltaic semiconductor devices is a complex task and varies greatly depending on the photodiode architecture. In a classical p-n junction, the non-ideality factor (**m**) equals 1 when diffusion current predominates over recombination current. The parameter can reach a value of 2 when recombination current dominates in the space charge region. A lower non-ideality factor indicates reduced recombination

dynamics and increased efficiency of the junction for charge carrier transport. A lower non-ideality factor points to reduced recombination dynamics and increased junction efficiency for charge carrier transport. P-i-n diode devices based on halide perovskites are more complex, involving two hetero-junctions. Therefore, recombination processes in PPDs are not described by the *m* range of 1-2 and require modification of standard equivalent electrical circuits. In our work, we used a 2-diode model with diodes in series, calculating the non-ideality factor as the sum of the values of each diode. For the control sample, the calculated non-ideality factor was 2.811. In the Bulk configuration, the value significantly decreased to 1.792, demonstrating notable changes in recombination processes associated with the interfaces of the microcrystalline perovskite film. Interestingly, the non-ideality factor for the Bulk/n-type configuration, while lower than the control at 2.610, exceeded the Bulk device values. Potential losses in charge carrier transport efficiency could be attributed to the non-optimized P(VDF-TrFE) deposition process on the surface.

Table 2. Calculated parameters for fitted dark JV curves

Device configuration	**m_1**	**m_2**	**m (m_1+m_2)**	**J_{01}, A*cm^{-2}**	**J_{02}, A*cm^{-2}**	**R_{sh}, ohm*cm^2**
Control	1.534	1.277	2.811	1.34E-12	8.78E-4	3.66E+04
Bulk	1.112	0.680	1.792	1.72E-13	3.17E-6	5.58E+04
Bulk/n-type	1.320	1.290	2.610	3.03E-11	6.66E-8	1.62E+06

The photo-response of PPDs in short-circuit and open-circuit modes was assessed over a wide range of illumination power densities (P_0, 540 nm, LED source, range: 10^{-3} to 10^{1} mW/cm², **fig.4**). For the short-circuit current (J_{sc}), linear trends were observed, as the photocurrent ∝ charge generation rate. The calculation of the responsivity (**R, eq.S12** in **ESI**), representing photocurrent dependence on P_0 at a wavelength of 540 nm, resulted in values of 0.32 A/W for the control device, 0.38 A/W for the Bulk, and 0.44 A/W for the Bulk/n-side configuration. The dependence of open-circuit voltage (V_{oc}) vs. P_0 exhibited a logarithmic nature. The Bulk/n-side modification of the device increased V_{oc} across the full range of light intensities by 0.02 to 0.05 V compared to control PPDs. On the other hand, Bulk devices showed the highest V_{oc} values at low-light intensities (<10^{-1} mW/cm²), indicating changes in the separation and collection of the charge carriers.

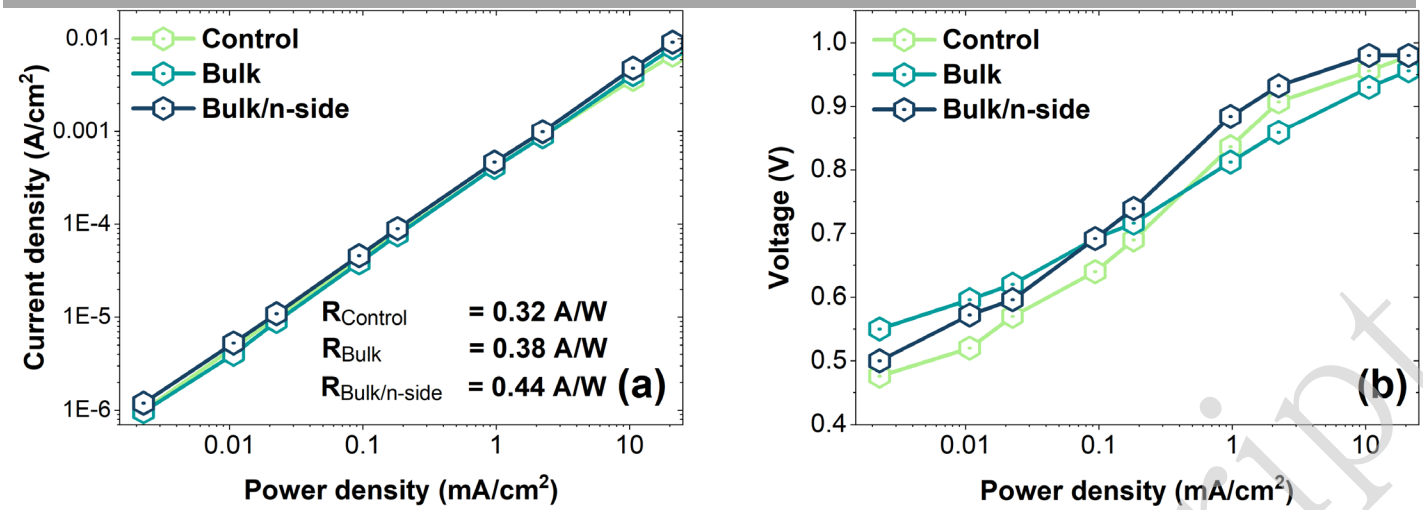

Figure 4 – The linearity plot of J_{sc} to P_0 for the various perovskites modifications on a logarithmic scale (a); the dependence of V_{oc} vs. P_0 on a semi-logarithmic scale (b)

For the illumination power density range used, we calculated the linear dynamic range (LDR, eq. **S13** in ESI), which defines the range of incident light power over which the photodiode output current depends linearly on the input optical power. This critical characteristic determines the photodiode's ability to accurately measure light intensity over a wide range of power levels. Calculations of LDR values under 540 nm LED illumination indicated an increase from 76.6 dB to 99.5 dB for PPDs with P(VDF-TrFE) interlayers (**tab.3**). This originated from the reduction in dark current and the improvement in the signal-to-noise ratio for the Bulk and Bulk/n-side configurations. Across the P_0 range from 10^{-3} to 10^{1} mW/cm², we observed no deviation from linearity in the photocurrent, suggesting that the LDR values for the designed PPDs may potentially exceed 100 dB. The spectral performance of the devices was estimated via measurements of the external quantum efficiency (**fig.S6** in **ESI**). All PPD configurations exhibited a high level of photoelectric conversion, between 82% and 87%, in the visible part of the spectrum. This correlates with the data obtained under high optical pumping conditions (540 nm).

Based on the assumption that shot noise is dominant in PPDs, we estimated the key figures of merit parameters—specific detectivity (**D***) and noise equivalent power (**NEP**)—for the short-circuit mode (zero bias). The data calculated using **eq. S14, S15** (**ESI**) are presented in **tab.3**. Reducing current leakage in devices with modified interfaces increased D* by almost an order of magnitude, approaching the value of 10^{12} Jones for the Bulk/n-side configuration. Strengthening the shunt properties and increasing R led to a reduction in the NEP for the P(VDF-TrFE)-containing devices. While the NEP for the control sample was around ~10^{-12} W·Hz$^{-1/2}$, we obtained 6.6×10^{-13} and 4.00×10^{-13} W·Hz$^{-1/2}$ for the Bulk and Bulk/n-side configurations, respectively.

Table 3. Calculated D* and NEP for the fabricated PPDs

Device	LDR (dB)	D* (Jones) at 540 nm	NEP (W·Hz$^{-1/2}$)
Control	76.6	$2.20\cdot10^{11}$	$1.76\cdot10^{-12}$

Bulk	92.0	$5.78 \cdot 10^{11}$	$6.65 \cdot 10^{-13}$
Bulk/n-side	99.5	$9.69 \cdot 10^{11}$	$4.00 \cdot 10^{-13}$

We compared the performance of PPDs from our work with state-of-the-art devices (**Tab. S1** in **ESI**). The D* parameters for the Bulk and Bulk/n-side configurations are relevant when compared to other perovskite photodiode modifications, where the typical range is between 10^{10} and 10^{14} Jones. Moreover, our work demonstrates competitive values for NEP and response time.

Perovskite devices with diode structure are known to exhibit hysteresis[19,63,64] caused by ion migration and accumulation at the interfaces, resulting in dynamic capacitance changes, gating, and zone bending. We conducted hysteresis measurements under monochromatic LED illumination (540 nm, 0.62 mW/cm²) and cycled IV scans from open-circuit to 0 V (short-circuit). Five cycles were performed for each device type, with the IV curves shown in (**Fig. S7**, **ESI)**. The hysteresis index (HI, **tab.S2**, **ESI**), was calculated using formula **S16** (**ESI**), was used to assess the effect by shifts of the diode's maximum power point. Notably, for control devices we obtained enhanced shifts of the working point (maximum power) and V_{oc}, while Bulk and Bulk/n-side devices these effects were slightly suppressed. For the first cycle of measurements Control device showed the highest value of HI (14%), while Bulk and Bulk/n-side devices exhibited reduced values of 8-11%. During the cycles PPDs showed a similar trend for increase of HI. The integration of ferroelectric material at low concentrations did not contribute to accumulation effects or additional ion migration.

To assess the response dynamics of PPDs, we measured the transient characteristics of ON/OFF modes during optical pumping (**fig.5**). A square pulse of light (LED, 50 kHz) was used to evaluate changes in the rise and fall profiles of the photocurrent over time. Specifically, we analyzed the rise and fall times ($\mathbf{t_r}$ and $\mathbf{t_f}$) of the current response at amplitudes corresponding to 10% and 90% of signal saturation. The devices exhibited a characteristic π-shaped waveform. For the control device, the t_r was 6.3 μs, and the t_f was 10.9 μs. Bulk PPDs demonstrated enhanced performance with decreased transient times: t_r = 4.9 μs (-22.6%) and t_f = 6.7 μs (-15.6%). The Bulk/n-side configurations showed the most rapid signal growth profile with t_r = 4.6 μs (-32.6%), while decay was 6.5 μs. The box—charts for data of t_r and t_f for PPDs presented in the **fig. S8** (**ESI**), which represents clear correlation between time of the response and

configuration of the devices.

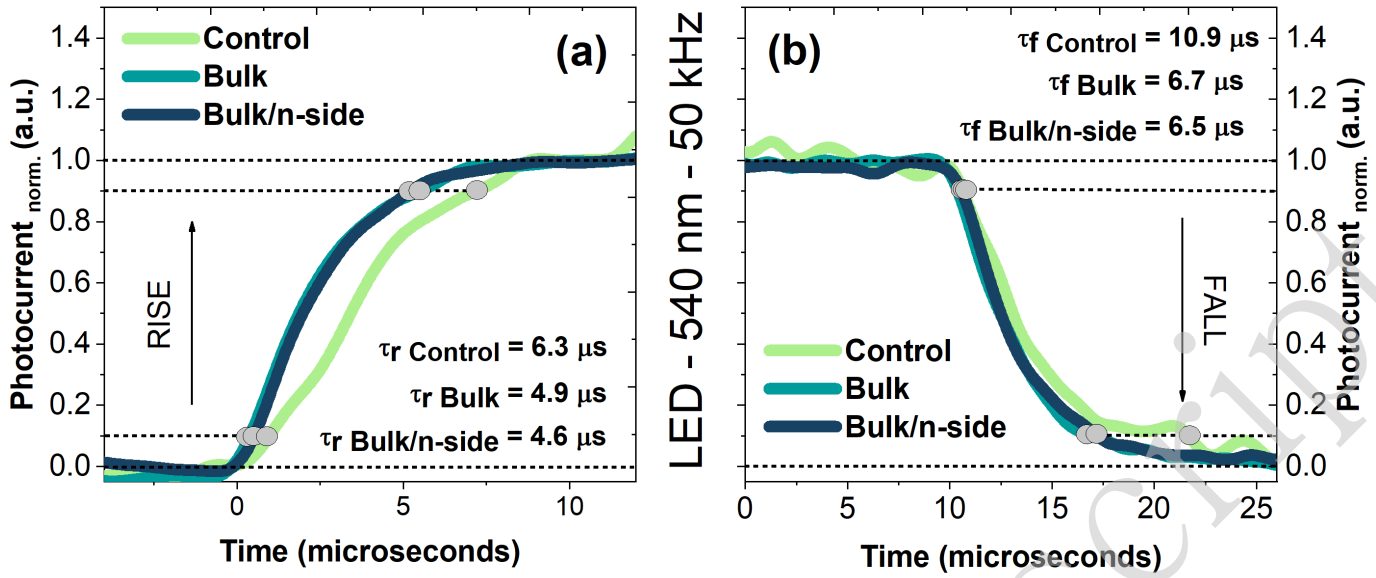

Figure 5 – Response dynamics in rise (a) and fall (b) modes for the control device; PPDs of Bilk and Bulk/n-side configurations

A crucial parameter of the photodiode related to photo-response dynamics is the cut-off frequency, defined as the frequency at which the photodiode's response diminishes to 3 dB below its maximum value ($\mathbf{f_{3dB}}$). This parameter determines the speed at which the photodiode can respond to the relevant changes in the light signal. The 3 dB point corresponds to a power reduction of half of its maximum value or a decline in current to 0.707 from the maximum. Essentially, f_{3dB} sets the upper limit on the frequency of the light signal that the photodiode can efficiently detect. For f_{3dB} measurements, the amplitude of the photodiode photocurrent was measured when optically pumped with a square pulse of a green LED (540 nm) at different frequencies of the LED glow. Measurements were carried out for the frequency range from 10 to 90 kHz. The illumination was carried at a power density of 2 mW/cm^2. The measured data is presented in **fig.6**. Enhanced speed and transport performance in the PPDs, containing P(VDF-TrFE), increased the f_{3db} from 64.8 kHz for the control device to 71.9 kHz and 76.8 kHz for the Bulk and Bulk/n-side configurations, respectively. To evaluate the stability of the devices, we measured the transient characteristics after 250 hours of thermal stress (70°C) (**fig.S9** in **ESI**). For all PPDs configurations, the decrease in response speed was negligible. Also, we estimated the stability of the devices by monitoring changes in dark current during prolonged exposure to high humidity conditions (60-80%), as well as during ON/OFF cycling. After 36 million ON/OFF cycles, we observed negligible changes in the rise and fall signals. The storage in the high-humidity conditions also didn't affected the dynamics of the photo-response (**fig.S10 – S12**, **ESI**).

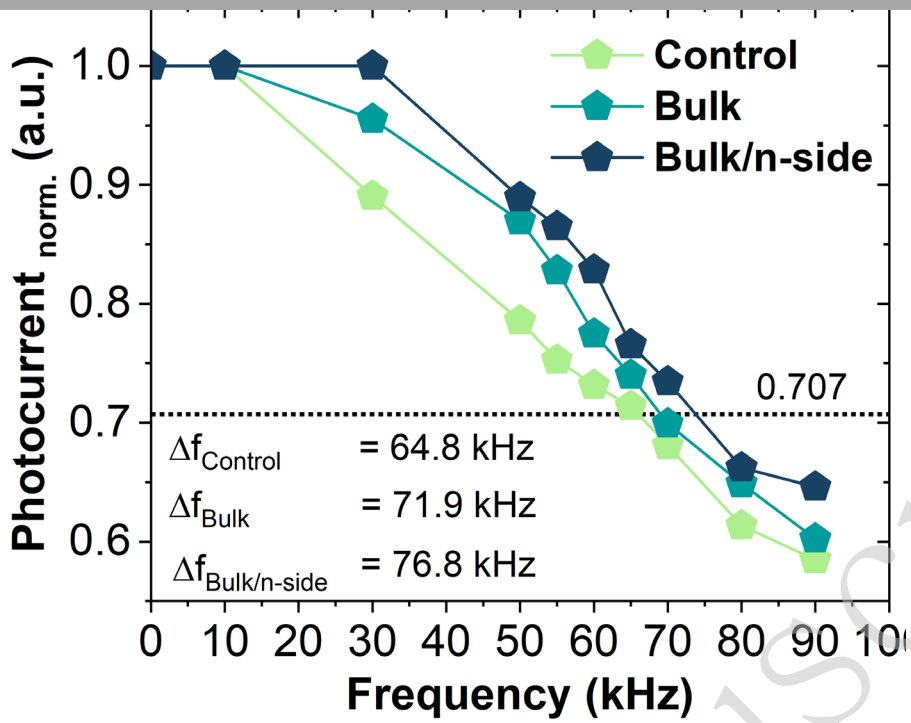

Figure 6 – F_{3db} bandwidth for the fabricated PPDs with dielectric interlayers

We utilized Photo-Induced Voltage Spectroscopy (PIVTS) [55] and Admittance Spectroscopy (AS) to conduct an in-depth evaluation of Fermi level shifts and trap state contributions. The principle of PIVTS involves monitoring V_{oc} under impulse light pumping (square LED pulses, 470 nm) and analyzing relaxation kinetics during signal decay over a wide temperature range (190-360K). Upon illumination, the perovskite photodiode reaches a steady-state V_{oc} and saturates after turn-on. Upon turning off the light, non-equilibrium charge carriers recombine over their characteristic lifetimes (typically within nanoseconds to tens of nanoseconds), leading to a decay in V_{oc}. Perovskite devices exhibit unique behavior due to the slow migration of ionic defects and their associated electric fields [65,66]. By analyzing the PIVTS relaxation spectra, we can reveal the kinetics of trapping processes across different temperature intervals. We conducted combined PIVTS and AS measurements for the PPDs, with the data presented in **Fig. S13** (**ESI**).

PIVTS analysis demonstrated that the introduction of P(VDF-TrFE) led to a reconfiguration of defect states. In the Control device, high amplitude signals were observed within the temperature range of 275-320 K, near room temperature and within the typical operating range for photodiodes. The contribution of ionic species can be linked to defect activation energies reported in the literature[67–69]. However, identifying the precise nature of these defects is a complex task, as various factors—such as crystallization methods[17] and doping[70]—affect their numerical parameters. In the Control device, a defect center α, with an activation energy of 0.72 eV, was observed. This defect may correspond to the position of the iodine anion in the perovskite structure[16], such as iodine in an interstitial site (I_i) or an antisite with lead (I-Pb)[69]. Similar energies were observed for the Bulk and Bulk/n-side devices, but at reduced temperatures (250-300 K). The amplitude of the α-defect signal was diminished in PPDs containing P(VDF-TrFE). At higher temperatures, a deep β-center signal emerged, which is uncommon for $CsFAPbI_3$ and might correspond to an anti-site state

of the organic cation (A-site)[71]. Admittance spectroscopy analysis showed that ionic species concentrations for all PPD configurations were approximately 10^{16} cm^{-3}. These findings indicate that the introduction of P(VDF-TrFE) reconfigures defect states, reducing the α-center (E_a~0.7-0.8 eV) and introducing β-centers. Given the improved performance of P(VDF-TrFE)-based PPDs, it can be interpreted that α-defects play a critical role for $CsFAPbI_3$ properties in photodiodes application.

To investigate the potential interactions between PVDF-TrFE and the perovskite material, Fourier-transform infrared spectroscopy (FTIR) studies were conducted to demonstrate the interactions between the fluorinated fragments of the polymer and formamidinium iodide (see **Fig. S14, ESI** and a brief discussion therein). Previous studies have observed similar interactions between the fluorinated additive and FAI, resulting in a reduction in defects in the resulting formamidinium lead halides[72].

Our data on stability performance indicated no substantial degradation impact for soft exploitation conditions of PPDs. In this study, we employed double-cation perovskite $CsFAPbI_3$, which demonstrated relevant stability[73] for several thousand hours under conditions of constant light-soaking (100 mW/cm²) and heating (65°C). However, full stabilization of such perovskites compositions and device structures has not yet been confirmed. We analyzed the PIVTS results to evaluate the potential influence of P(VDF-TrFE) on the stabilization of PPDs against intrinsic factors. The degradation of halide perovskite-based devices is largely attributed to the decomposition of the perovskite absorber and the migration of the ionic defects [74,75]. Different nature of the defects could trigger specific degradation pathway. For FA-cation perovskites, I_i induces the transition from the cubic photoactive phase to the tetragonal inactive phase and accelerates the formation of neutral I_2 (filling of two traps)[76]. Charged antisites (such as I-Pb) could act as recombination centers and migrate to the metal electrode under electric field [21,77] The accumulation of the ionic defects at the interface typically induces corrosion processes associated with electrochemical oxidation[78]. PIVTS results revealed a decreased amplitude of the α-defect (0.7-0.8 eV) signals for PPDs with P(VDF-TrFE). Thus, we can conclude that the integration of P(VDF-TrFE) mitigates the corrosion dynamics driven by iodine-related defects and could enhance the long-term stabilization of PPDs. The obtained data on defect activation energies suggest that the Fermi level pinning may be caused by complex factors, including point defects related to iodine or organic cations.

This work presents a solution-processed approach for integrating an organic dielectric into the volume and interfaces of a perovskite absorber. The complementary solubility and selected dielectric concentrations have a significant impact on device performance. However, the method is not fully universal, as it requires careful consideration of surface state modifications and energy level alignment specific to different materials. Furthermore, we conducted an additional experiment to integrate P(VDF-co-CTFE)-graft-PEMA dielectric using a process similar to that employed for P(VDF-TrFE). P(VDF-co-CTFE)-g-PEMA represents an analogue of P(VDF-TrFE), comprising grafted chains of polyethyl methacrylate (PEMA). The synthesis of P(VDF-co-CTFE)-g-PEMA has been previously described by our group[79]. P(VDF-CTFE)-g-PEMA has a high melting point of 160°C and a decomposition temperature above 390°C, whether in air or inert atmospheres [79]. It has a permittivity of approximately 7, conductivity around 10^{-12}

S/cm, and a dielectric loss factor of about 10[79]. The incorporation of PEMA chains into the copolymer structure enhances the solubility of PVDF-based polymeric dielectrics in the solvents typically employed for perovskite layer preparation. Additionally, non-covalent interactions, including those between the perovskite and the carbonyl groups of PEMA, may potentially occur as compared to P(VDF-TrFE).

We evaluated the impact of P(VDF-co-CTFE)-g-PEMA integration on the transport and spectral properties of PPDs. Dark JV measurements indicated that P(VDF-co-CTFE)-g-PEMA integration in Bulk and Bulk/n-side configurations weakened shunt properties and increased leakage current, with $J_{leakage}$ values around ~$9x10^{-5}$ A/cm² for the Bulk configuration and rising to ~$3x10^{-2}$ A/cm² for Bulk/n-side (**fig.S15(a)**, **ESI**). The calculated R_{sh} values for P(VDF-co-CTFE)-g-PEMA remained under 1 kOhm-cm². Despite this degradation in diode properties, the alternative dielectric affected the EQE (**fig.S15(b)**, **ESI**). Compared to PPDs utilizing P(VDF-TrFE), the alternative configurations exhibited a slight reduction in photoelectric conversion between 300-550 nm, while significantly raising the spectra shoulder in the 750-800 nm region. In perovskite-based p-i-n diodes, high-energy photons are absorbed in the frontal regions near the HTL/absorber interface, with conversion determined by EQE at shorter wavelengths. The increased EQE in the infrared region suggests improved electron collection efficiency, a distinctive feature of P(VDF-co-CTFE)-g-PEMA integration. However, the strong increase in leakage current prevented any notable improvement in output performance (**Fig.S16** in **ESI**) for J_{sc} vs P_o and V_{oc} vs P_o dependencies. These approaches reveal critical dielectric properties for modifying perovskite layer interfaces at low concentrations. The molecular design of the dielectric must accommodate energy level alignment, neutralize surface states, and ensure layer continuity after crystallization. Through this comparative experiment between P(VDF-co-CTFE)-g-PEMA and P(VDF-TrFE), we have demonstrated that materials with similar molecular structures can produce significantly different outcomes in diode and spectral performance.

The integration of P(VDF-TrFE) dielectric materials has been demonstrated to be effective for perovskite-based diode structures. In early works [80,81], researchers utilized P(VDF-TrFE) to enhance the built-in electric field within perovskite absorbers, thereby improving the collection efficiency of the free charge carriers. However, the previously presented approaches relied on poling effects, which potentially initiate ion migration processes under polarization conditions. Polling and migration effects can adversely affect device performance. In our work, we have demonstrated an approach involving complex modification of interfaces within the bulk and at the electron collection junction, wherein P(VDF-TrFE) primarily compensates for charge carrier traps. PPDs-containing incorporating P(VDF-TrFE) in the bulk absorber and at bulk/n-type interfaces operated in regimes similar to reference devices and didn't require pre-conditioning. We observed a relevant increase in photo-carrier lifetime with the integration of P(VDF-TrFE) on the perovskite film surface, indicating a influence of the dielectric interlayer on recombination processes and charge carrier splitting. A comprehensive analysis of diode transport characteristics also shows a reduced contribution of non-radiative recombination at the interfaces for the devices with dielectric interlayers. P(VDF-TrFE) plays a significant role in enhancing the shunt properties of PPDs and reducing

dark currents. The presence of a thin dielectric layer assists in mitigating potential defects in morphology, such as micro-pinholes. This correlates with the measured photo-response of PPDs. The increase in **R** is linked to better photo-carrier collection efficiency (see **eq.S17** in **ESI**)[82]. The rise in V_{oc} in low light intensity regions results from improved energy level alignment and reduced trap-states in the band-gap, which negatively impact quasi-Fermi level splitting[83] during photo-injection. Improved dynamic performance is a key result of this work. The photo-response profile directly correlates with the cut-off frequency. Different capacitive effects according to multiple models [19,84,85] describe variations in transition time in perovskite diode architectures. The appearance of slow components in the transient photocurrent (as observed in the PPD control) is typically associated with the accumulation of ionic species at interfaces [86–88], which in a perovskite photodiode can be represented by iodine vacancies, uncompensated organic cation ions, iodine in interstitials, etc. The photodiode junction capacitance, combined with other capacitances in the circuit, forms an RC constant with the load resistance, which limits the device's bandwidth. The charge-carrier transit time and RC constant determine the cut-off frequency (**eq.1**) [89–91].

$$f_{-3dB}^{-2} = \left(\frac{3.5}{2\pi t_{CCT}}\right)^{-2} + \left(\frac{1}{2\pi RC}\right)^{-2} \quad (1)$$

Where t_{CCT} - charge-carrier transit time

R - total series resistance, including the device resistance, contact resistances, and load resistances

C - the sum of the capacitance of the device

The improvements in dynamic response for the Bulk/n-side configuration result from a complex interplay of suppressed trapping, reduced accumulation effects, and minimized current leakage. Compared to similar studies on integrating dielectrics into the absorber volume and interfaces of a perovskite photodiode[81,92–94], our results demonstrate superior f_{3}dB and improved transition times.

To demonstrate the practical value of interface engineering using organic dielectrics, we conducted measurements using a setup comprising an X-ray tube (RAD-160 system, tungsten tube) and a scintillator (CsI bar, **fig. 7(a)**). The photoelectric conversion of visible scintillation light by photodiodes is a common application for string and array devices[95]. Non-direct detector systems[96] operates by integrating photodiodes with scintillators, such as CsI, which emit green light (~520 nm) upon absorbing ionizing radiation[97]. We employed a tungsten tube-based X-ray source with a commercial CsI bar as the scintillator and placed a substrate with photodiode pixels behind it (photo-image of setup presented in **fig. S17**, **ESI**). To assess performance differences, we measured the amplitude of the transient current signal under X-ray exposure at 160 kV tube voltage and 1 mA tube current. The transient signal profiles for the PPDs are displayed in **Fig. 7(b)**. The signal buildup over a few milliseconds is attributed to the slow emission buildup of the X-ray tube, while the CsI luminescence time is in the nanosecond range[98], and the fast PPD performance was measured in microseconds. Analysis of the signal rise profiles from the scintillator light revealed that the photo-response amplitude increased significantly for Bulk and Bulk/n-side samples

compared to the Control. The signal-to-noise ratios (SNR) were 27 for Control, 46 for Bulk, and 57 for Bulk/n-side. So, the improvements in the specific detectivity with enhanced diode properties, validate the efficiency of interface engineering in practical applications.

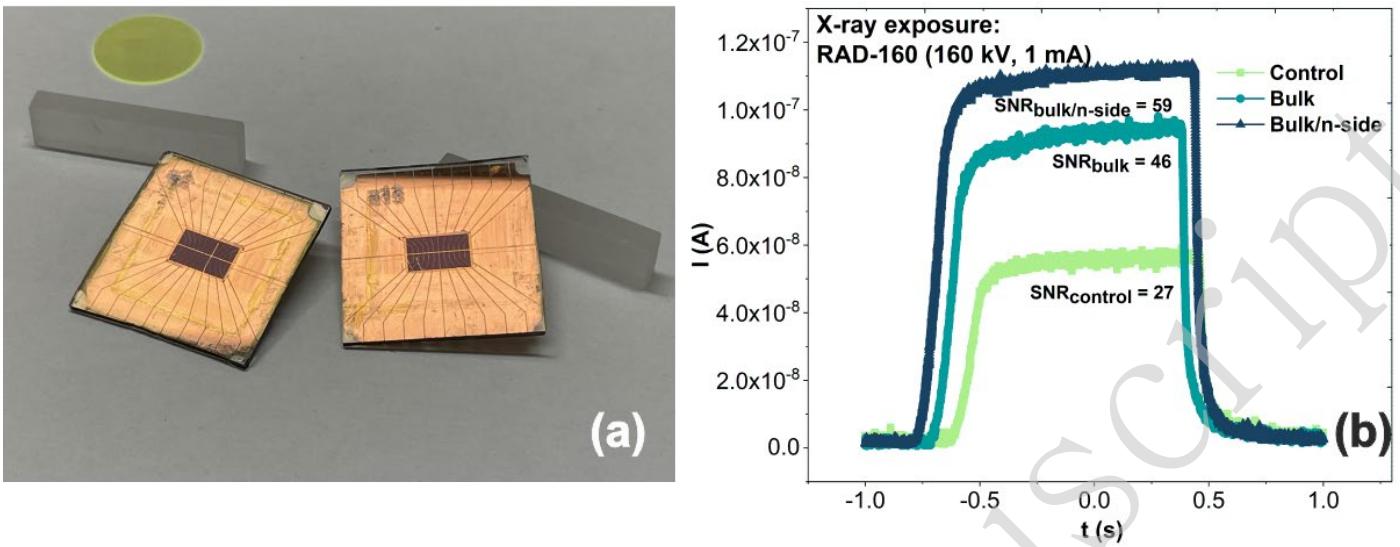

Figure 7 – Photo-image of the PPDs fabricated as a stroke of 10 pixels (a); SNR for PPDs measured for conversion of scintillating CsI light induced by X-ray flux (tungsten tube source) (b). The signal profiles correspond to the switch-on regime of X-Ray source

Our method for manufacturing photodiodes can be scaled up to large-area arrays, with dimensions extending to tens of square centimeters, for example, in the development of flat-detector panels[99]. A layer-by-layer coating can be achieved using slot-die cycles[100], a process well-established in solar module fabrication. The patterning of large-area photodiode arrays can be completed with multistep laser scribing[101]. In the Bulk configuration, P(VDF-TrFE) is combined with absorber deposition/crystallization. In the case of the n-side configuration, up-scaling requires the selection of a complementary solvent that prevents interaction with the absorber, or alternatively, ultrafast deposition followed by rapid drying. We assume that Bulk device configuration with P(VDF-TrFE) could also be effectively utilized in n-i-p device architectures[102] or even tandems[103] without major up-grades, as the solvents for the dielectric and perovskite solutions are complementary. On the other hand, adapting the n-side modification for n-i-p structures should account for possible changes in the wetting properties of the ETL. F-atom-rich P(VDF-TrFE) on the ETL's surface could increase the surface wetting angle and result in void formation[104] after absorber crystallization.

Conclusions

In this work, we performed a comprehensive study of P(VDF-TrFE) integration in bulk of the absorber and electron transport surfaces for PPDs. We demonstrated that dielectric incorporation provides Fermi level pinning, shifting it from 4.85 eV for bare $CsFAPbI_3$ to 4.16-4.28 eV. This adjustment reconfigures the energy level alignment that potentially allows more efficient electron collection. The

Bulk/n-side configuration exhibited beneficial improvements in the entire spectra of photodiode performance parameters. This underscores the benefits of a complex modification of both the microcrystalline absorber and hetero boundaries with standard transport layers like C_{60} fullerenes. Integration at low concentrations compensated charged ionic defects linked to the molecular position of iodine, leading to improved diode properties. Furthermore, the ferroelectric nature of P(VDF-TrFE) doesn't result in undesirable hysteresis or accumulation effects. The dielectric interface layers reduced the non-ideality factor and dark leakage currents. The responsivity of the fabricated PPDs was 0.32 A/W for the control device, 0.38 A/W for the Bulk, and 0.44 A/W for the Bulk/n-side configuration. Reducing the impact of non-radiative recombination processes at the interfaces allowed to decrease the NEP to ~10^{-13} $W \cdot Hz^{-1/2}$ and achieve a relevant D* of ~10^{12} Jones. Despite the meaningful differences in the photo response (I_{sc} vs P_o, V_{oc} vs P_0) between bulk and Bulk/n-side devices, the dynamic response showed close behavior. The cut-off frequency was increased from 64.8 (control) to 71.9 (Bulk) and 76.8 kHz (Bulk/n-side). Photodiodes with f_3dB values between 50 - 100 kHz are considered for use in applications that don't require extra fast response (GHz range), such as light measurement and sensing in industrial or scientific equipment, optical switches and encoders, low-speed optical communication systems, some types of the optical remote controls. This paper demonstrates the importance of complex interface processing in perovskite photodiodes, with a focus on the unique bulk modification and heterojunction with electron-transport layers. The developed method of using dielectrics combines the efficient tuning of transport properties and fast performance. Our work provides new insights into interface engineering for perovskite optoelectronics, aiming to comprehensively enhance the output performance.

SUPPLEMENTARY MATERIAL

The supplementary material includes description of the materials section (materials, inks preparation, device fabrication, characterization), details for the double diode model used for fitting of dark JV curves, external quantum efficiency spectra, and transient response after heat-stress and ON/OFF cycles.

The data that supports the findings of this study are available within the article and its supplementary material

Acknowledgments

The authors gratefully acknowledge the financial support from Russian Science Foundation with project № 22-19-00812.

Author contributions

D.S.S. and Yu.N.L. conceived the work.

Yu.N.L. and I.V.D. provided polymer dielectric materials.

A.P.M., S.Yu.U., P.A.G., S.I.D., E.A.I. performed device characterization and IV modelling

L.O.L., D.S.M., **N.S.S., D.O.B., N.S.S.** performed advanced characterization of surface and optical properties.

A.A.R, A.A.V. performed PIVTS and AS analysis.

D.S.S. and Yu.N.L. provided administrative support and resources.

The manuscript was written with contributions from all the authors. All the authors approved the final version of the manuscript.

References

1. Wu, Y. et al. Halide perovskite: a promising candidate for next-generation X-ray detectors. *Advanced Science* **10**, 2205536, doi: 10.1002/advs.202205536 (2023).
2. Wang, H. Y. et al. A review of perovskite-based photodetectors and their applications. *Nanomaterials* **12**, 4390 (2022).
3. Yaghoobi Nia, N. et al. Perovskite solar cells. in Solar Cells and Light Management (eds Enrichi, F. & Righini, G. C.) (Amsterdam: Elsevier, 2020), 163–228.
4. Tang, Z. K. et al. Enhanced optical absorption via cation doping hybrid lead iodine perovskites. *Scientific Reports* **7**, 7843 (2017).
5. Chen, Z. L. et al. Thin single crystal perovskite solar cells to harvest below-bandgap light absorption. *Nature Communications* **8**, 1890 (2017).
6. Motta, C., El-Mellouhi, F. & Sanvito, S. Charge carrier mobility in hybrid halide perovskites. *Scientific Reports* **5**, 12746, doi: 10.1038/srep12746 (2015).
7. Kulkarni, S. A. et al. Band-gap tuning of lead halide perovskites using a sequential deposition process. *Journal of Materials Chemistry A* **2**, 9221-9225 (2014).
8. Amat, A. et al. Cation-Induced band-gap tuning in organohalide perovskites: interplay of spin–orbit coupling and octahedra tilting. *Nano Letters* **14**, 3608-3616 (2014).
9. Ollearo, R. et al. Multidimensional perovskites for high detectivity photodiodes. *Advanced Materials* **34**, 2205261, doi: 10.1002/adma.202205261 (2022).
10. Wu, D. et al. Universal strategy for improving perovskite photodiode performance: interfacial built‐in electric field manipulated by unintentional doping. *Advanced Science* **8**, 2101729, doi: 10.1002/advs.202101729 (2021).

11. Le, T. S. et al. All‐slot‐die‐coated inverted perovskite solar cells in ambient conditions with chlorine additives. *Solar RRL* **6**, 2100807 (2022).

12. Zhang, L. H. et al. Ambient inkjet‐printed high‐efficiency perovskite solar cells: manipulating the spreading and crystallization behaviors of picoliter perovskite droplets. *Solar RRL* **5**, 2100106 (2021).

13. Cai, M. L. et al. Cost‐performance analysis of perovskite solar modules. *Advanced Science* **4**, 1600269, doi: 10.1002/advs.201600269 (2017).

14. Brandt, R. E. et al. Searching for “Defect-Tolerant” photovoltaic materials: combined theoretical and experimental screening. *Chemistry of Materials* **29**, 4667-4674 (2017).

15. Azarhoosh, P. et al. Research update: relativistic origin of slow electron-hole recombination in hybrid halide perovskite solar cells. *APL Materials* **4**, 091501 (2016).

16. Xue, K. et al. Defect investigation in perovskite solar cells by the charge based deep level transient spectroscopy (Q-DLTS). Proceedings of International Conference on Advances in Engineering Research and Application. Cham: Springer, 2019. 204-209.

17. Vasilev, A. A. et al. Deep-level transient spectroscopy of the charged defects in p-i-n perovskite solar cells induced by light-soaking. *Optical Materials*: *X* **16**, 100218 (2022).

18. Shikoh, A. S. et al. Ion dynamics in single and multi-cation perovskite. *ECS Journal of Solid State Science and Technology* **9**, 065015 (2020).

19. Gonzales, C., Guerrero, A. & Bisquert, J. Transition from capacitive to inductive hysteresis: a neuron-style model to correlate *I–V* curves to impedances of metal halide perovskites. *The Journal of Physical Chemistry C* **126**, 13560-13578 (2022).

20. Park, J. S. et al. Accumulation of deep traps at grain boundaries in halide perovskites. *ACS Energy Letters* **4**, 1321-1327, doi: 10.1021/acsenergylett.9b00840 (2019).

21. Ni, Z. Y. et al. Evolution of defects during the degradation of metal halide perovskite solar cells under reverse bias and illumination. *Nature Energy* **7**, 65-73 (2022).

22. Di Girolamo, D. et al. Stability and dark hysteresis correlate in NiO‐based perovskite solar cells. *Advanced Energy Materials* **9**, 1901642 (2019).

23. Chen, B. et al. Imperfections and their passivation in halide perovskite solar cells. *Chemical Society Reviews* **48**, 3842-3867, doi: 10.1039/c8cs00853a (2019).

24. Uratani, H. & Yamashita, K. Charge carrier trapping at surface defects of perovskite solar cell absorbers: a first-principles study. *The Journal of Physical Chemistry Letters* **8**, 742-746 (2017).

25. Sherkar, T. S. et al. Recombination in perovskite solar cells: significance of grain boundaries, interface traps, and defect ions. *ACS Energy Letters* **2**, 1214-1222 (2017).

26. Wang, D. D. et al. Interfacial passivation and energy level alignment regulation for self‐powered perovskite photodetectors with enhanced performance and stability. *Advanced Materials Interfaces* **9**, 2101766, doi: 10.1002/admi.202101766 (2022).

27. Lu, J. Y. et al. Back interface passivation for efficient low-bandgap perovskite solar cells and photodetectors. *Nanomaterials* **12**, 2065, doi: 10.3390/nano12122065 (2022).

28. Zhao, Y. et al. Surface passivation of $CsPbBr_3$ films by interface engineering in efficient and stable self-powered perovskite photodetector. *Journal of Alloys and Compounds* **965**, 171434, doi: 10.1016/j.jallcom.2023.171434 (2023).

29. Kim, W. et al. Highly efficient and stable self-powered perovskite photodiode by cathode-side interfacial passivation with poly(methyl methacrylate). *Nanomaterials* **13**, 619 (2023).

30. Choi, M. et al. Lithography-free broadband ultrathin-film absorbers with gap-plasmon resonance for organic photovoltaics. *ACS Applied Materials & Interfaces* **8**, 12997-13008 (2016).

31. He, G., Chen, X. S. & Sun, Z. Q. Interface engineering and chemistry of Hf-based high-k dielectrics on III–V substrates. *Surface Science Reports* **68**, 68-107 (2013).

32. Aguirre-Tostado, F. S. et al. S passivation of GaAs and band bending reduction upon atomic layer deposition of HfO_2/Al_2O_3 nanolaminates. *Applied Physics Letters* **93**, 061907, doi: 10.1063/1.2961003 (2008).

33. Lee, D. H. et al. A study of the surface passivation on GaAs and In/sub 0.53/Ga/sub 0.47/As Schottky-barrier photodiodes using SiO/sub 2/, Si/sub 3/N/sub 4/ and polyimide. *IEEE Transactions on Electron Devices* **35**, 1695-1696 (1988).

34. Yakusheva, A. et al. Photo stabilization of p-i-n perovskite solar cells with bathocuproine: MXene. *Small* **18**, 2201730, (2022).

35. Prateek, Thakur, V. K. & Gupta, R. K. Recent progress on ferroelectric polymer-based nanocomposites for high energy density capacitors: synthesis, dielectric properties, and future aspects. *Chemical Reviews* **116**, 4260-4317 (2016).

36. Khudyshkina, A. D. et al. Synthesis and characterization of polyacrylonitrile-grafted copolymers based on poly(vinylidene fluoride). *Express Polymer Letters* **15**, 957-971 (2021).

37. Kleimyuk, E. A. et al. Polyvinylidene fluoride copolymers with grafted polyethyl methacrylate chains: synthesis and thermal and dielectric properties. *Polymer Science*, *Series C* **64**, 200-210 (2022).

38. Chen, X., Han, X. & Shen, Q. D. PVDF‐based ferroelectric polymers in modern flexible electronics. *Advanced Electronic Materials* **3**, 1600460, doi: 10.1002/aelm.201600460 (2017).

39. Jia, E. D. et al. Efficiency enhancement with the ferroelectric coupling effect using P(VDF‐TrFE) in $CH_3NH_3PbI_3$ solar cells. *Advanced Science* **6**, 1900252, doi: 10.1002/advs.201900252 (2019).

40. Cao, F. R. et al. Ultrahigh‐performance flexible and self‐powered photodetectors with ferroelectric P(VDF‐TrFE)/perovskite bulk heterojunction. *Advanced Functional Materials* **29**, 1808415, doi: 10.1002/adfm.201808415 (2019).

41. Wang, S. S. et al. Polymer strategies for high-efficiency and stable perovskite solar cells. *Nano Energy* **82**, 105712 (2021).

42. Wu, Z. F. et al. Passivation strategies for enhancing device performance of perovskite solar cells. *Nano Energy* **115**, 108731 (2023).

43. Aggarwal, Y. et al. Highly efficient self-powered $CH_3NH_3PbI_3$ perovskite photodiode with double-sided poly(methyl methacrylate) passivation layers. *Solar Energy Materials and Solar Cells* **270**, 112815 (2024).

44. Ri, J. H. et al. Effect of polyethylene glycol as additive for fully screen-printable perovskite solar cells. *Journal of Electronic Materials* **49**, 7065-7071 (2020).

45. Sathiyan, G. et al. Impact of fluorine substitution in organic functional materials for perovskite solar cell. *Dyes and Pigments* **198**, 110029 (2022).

46. Sun, R. M. et al. Over 24% Efficient poly(vinylidene fluoride) (PVDF)‐coordinated perovskite solar cells with a photovoltage up to 1.22 V. *Advanced Functional Materials* **33**, 2210071, doi: 10.1002/adfm.202210071 (2023).

47. Liu, Y. et al. Ultrahydrophobic 3D/2D fluoroarene bilayer-based water-resistant perovskite solar cells with efficiencies exceeding 22%. *Science Advances* **5**, doi: 10.1126/sciadv.aaw2543 (2019).

48. Jiang, W. et al. Fluorine-containing cyclic surface passivators for perovskite solar cells with improved efficiency and stability. *Organic Electronics* **122**, 106879 (2023).

49. Wang, S. & Li, Q. Design, synthesis and processing of PVDF‐based dielectric polymers. *IET Nanodielectrics* **1**, 80-91 (2018).

50. Nie, J. H. et al. Piezophototronic effect enhanced perovskite solar cell based on P(VDF‐TrFE). *Solar RRL* **5**, 2100692, doi: 10.1002/solr.202100692 (2021).

51. Gallet, T. et al. Fermi-level pinning in methylammonium lead iodide perovskites. *Nanoscale* **11**, 16828-16836 (2019).

52. Sotthewes, K. et al. Universal fermi-level pinning in transition-metal dichalcogenides. *The Journal of Physical Chemistry C* **123**, 5411-5420 (2019).

53. Alkhalifah, G. et al. Defect-polaron and enormous light-induced fermi-level shift at halide perovskite surface. *The Journal of Physical Chemistry Letters* **13**, 6711-6720 (2022).

54. Walsh, A. et al. Self‐regulation mechanism for charged point defects in hybrid halide perovskites. *Angewandte Chemie International Edition* **54**, 1791-1794 (2015).

55. Shikoh, A. S. et al. On the relation between mobile ion kinetics, device design, and doping in double-cation perovskite solar cells. *Applied Physics Letters* **118**, 093501, doi: 10.1063/5.0037776 (2021).

56. Agresti, A. et al. Titanium-carbide MXenes for work function and interface engineering in perovskite solar cells. *Nature Materials* **18**, 1228-1234 (2019).

57. Saranin, D. et al. Transition metal carbides (MXenes) for efficient NiO-based inverted perovskite solar cells. *Nano Energy* **82**, 105771, doi: 10.1016/j.nanoen.2021.105771 (2021).

58. Di Vito, A. et al. Nonlinear work function tuning of lead-halide perovskites by mxenes with mixed terminations. *Advanced Functional Materials* **30**, 1909028 (2020).

59. Li, D. M. et al. New hole transporting materials for planar perovskite solar cells. *Chemical Communications* **54**, 1651-1654 (2018).

60. Al-Ashouri, A. et al. Monolithic perovskite/silicon tandem solar cell with >29% efficiency by enhanced hole extraction. *Science* **370**, 1300-1309 (2020).

61. Zhu, Z. L. et al. High‐performance hole‐extraction layer of sol–gel‐processed NiO nanocrystals for inverted planar perovskite solar cells. *Angewandte Chemie International Edition* **53**, 12571-12575 (2014).

62. Chen, W. et al. Understanding the doping effect on NiO: toward high‐performance inverted perovskite solar cells. *Advanced Energy Materials* **8**, 1703519, doi: 10.1002/aenm.201703519 (2018).

63. Snaith, H. J. et al. Anomalous hysteresis in perovskite solar cells. *The Journal of Physical Chemistry Letters* **5**, 1511-1515 (2014).

64. Tress, W. et al. Understanding the rate-dependent J–V hysteresis, slow time component, and aging in $CH_3NH_3PbI_3$ perovskite solar cells: the role of a compensated electric field. *Energy & Environmental Science* **8**, 995-1004 (2015).

65. Son, D. Y. et al. Universal approach toward hysteresis-free perovskite solar cell via defect engineering. *Journal of the American Chemical Society* **140**, 1358-1364, doi: 10.1021/jacs.7b10430 (2018).

66. Tumen-Ulzii, G. et al. Hysteresis-less and stable perovskite solar cells with a self-assembled monolayer. *Communications Materials* **1**, 31 (2020).

67. Pols, M. et al. Atomistic insights into the degradation of inorganic halide perovskite $CsPbI_3$: a reactive force field molecular dynamics study. *The Journal of Physical Chemistry Letters* **12**, 5519-5525 (2021).

68. Liu, N. & Yam, C. Y. First-principles study of intrinsic defects in formamidinium lead triiodide perovskite solar cell absorbers. *Physical Chemistry Chemical Physics* **20**, 6800-6804 (2018).

69. Deger, C. et al. Lattice strain suppresses point defect formation in halide perovskites. *Nano Research* **15**, 5746-5751 (2022).

70. Heo, S. et al. Deep level trapped defect analysis in $CH_3NH_3PbI_3$ perovskite solar cells by deep level transient spectroscopy. *Energy & Environmental Science* **10**, 1128-1133, doi: 10.1039/c7ee00303j (2017).

71. Tan, S., Huang, T. Y. & Yang, Y. Defect passivation of perovskites in high efficiency solar cells. *Journal of Physics*: *Energy* **3**, 042003 (2021).

72. Huang, Z. J. et al. Anion–π interactions suppress phase impurities in $FAPbI_3$ solar cells. *Nature* **623**, 531-537 (2023).

73. Gostishchev, P. et al. Cl‐anion engineering for halide perovskite solar cells and modules with enhanced photostability. *Solar RRL* **7**, 2200941 (2023).

74. Reichert, S. et al. Ionic-defect distribution revealed by improved evaluation of deep-level transient spectroscopy on perovskite solar cells. *Physical Review Applied* **13**, 034018 (2020).

75. Futscher, M. H. & Deibel, C. Defect spectroscopy in halide perovskites is dominated by ionic rather than electronic defects. *ACS Energy Letters* **7**, 140-144 (2022).

76. Motti, S. G. et al. Controlling competing photochemical reactions stabilizes perovskite solar cells. *Nature Photonics* **13**, 532-539 (2019).

77. Taufique, M. F. N. et al. Impact of iodine antisite (I_{Pb}) defects on the electronic properties of the (110) $CH_3NH_3PbI_3$ surface. *The Journal of Chemical Physics* **149**, 164704 (2018).

78. Li, X. D. et al. Chemical anti-corrosion strategy for stable inverted perovskite solar cells. *Science Advances* **6**, eabd1580, doi: 10.1126/sciadv.abd1580 (2020).

79. Khan, A. A. et al. Breaking dielectric dilemma via polymer functionalized perovskite piezocomposite with large current density output. *Nature Communications* **15**, 9511 (2024).

80. Du, Y. et al. A modulated heterojunction interface via ferroelectric P(VDF-TrFE) towards high performance quasi-2D perovskite self-powered photodetectors. *The Journal of Materials Chemistry A* **12**, 27518-27526 (2024.)

81. Luo, D. et al. Low-Dimensional Contact Layers for Enhanced Perovskite Photodiodes. *Advanced Functional Materials* **30**, 2001692, doi: 10.1002/adfm.202001692 (2020).

82. Zeiske, S. et al. Light intensity dependence of the photocurrent in organic photovoltaic devices. *Cell Reports Physical Science* **3**, 101096 (2022).

83. Caprioglio, P. et al. On the relation between the open‐circuit voltage and quasi‐fermi level splitting in efficient perovskite solar cells. *Advanced Energy Materials* **9**, 1901631, doi: 10.1002/aenm.201901631 (2019).

84. Bisquert, J., Gonzales, C. & Guerrero, A. Transient on/off photocurrent response of halide perovskite photodetectors. *The Journal of Physical Chemistry C* **127**, 21338-21350 (2023).

85. Ghahremanirad, E. et al. Inductive loop in the impedance response of perovskite solar cells explained by surface polarization model. *The Journal of Physical Chemistry Letters* **8**, 1402-1406 (2017).

86. Sakhatskyi, K. et al. Assessing the drawbacks and benefits of ion migration in lead halide perovskites. *ACS Energy Letters* **7**, 3401-3414 (2022).

87. Mahapatra, A. et al. Understanding the origin of light intensity and temperature dependence of photodetection properties in a $MAPbBr_3$ single-crystal-based photoconductor. *ACS Photonics* **10**, 1424-1433 (2023).

88. Ding, J. et al. Unraveling the effect of halogen ion substitution on the noise of perovskite single-crystal photodetectors. *The Journal of Physical Chemistry Letters* **13**, 7831-7837 (2022).

89. Kato, K. et al. Design of high-speed and high-sensitivity photodiode with an input optical waveguide on semi-insulating InP substrate. Proceedings of LEOS 1992 Summer Topical Meeting Digest on Broadband Analog and Digital Optoelectronics, Optical Multiple Access Networks, Integrated Optoelectronics, and Smart Pixels. Newport, RI, USA: IEEE, 1992, 254-257.

90. Armin, A. et al. Thick junction broadband organic photodiodes. *Laser & Photonics Reviews* **8**, 924-932 (2014).

91. Shen, L. et al. A self‐powered, sub‐nanosecond‐response solution‐processed hybrid perovskite photodetector for time‐resolved photoluminescence‐lifetime detection. *Advanced Materials* **28**, 10794-10800 (2016).

92. Kim, W. et al. Poly(amic acid)-Polyimide Copolymer Interfacial Layers for Self-Powered CH3NH3PbI3 Photovoltaic Photodiodes. *Polymers* **17(2)**, 163, (2025).

93. Yan, Y. et al. High Performance Perovskite Photodiodes via Molecule-Assisted Interfacial and Bulk Modulations. *Small* **4**, 2407015, doi: 10.1002/smll.202407015 (2024).

94. Song, W. et al. Halide Perovskite Photodiode Integrated CMOS Imager, *ACS Nano* **18**, 52 (2024).

95. Lecoq, P. Scintillation detectors for charged particles and photons. in Particle Physics Reference Library (eds Fabjan, C. W. & Schopper, H.) (Cham: Springer, 2020), 45-89.

96. Hou, B. et al. Materials innovation and electrical engineering in X-ray detection. *Nature Reviews Electrical Engineering* **1**, 639-655 (2024).

97. Lin, Z. Y. et al. Structured scintillators for efficient radiation detection. *Advanced Science* **9**, 2102439, doi: 10.1002/advs.202102439 (2022).

98. Belsky, A. N. et al. Excitation mechanisms of CsI fast intrinsic luminescence. *Journal of Luminescence* **72-74**, 93-95 (1997).

99. Khalil, T. et al. Review of flat panel detectors technique for medical imaging quality improvement. *AIP Conference Proceedings* **2307**, 020049 (2020).

100. Patidar, R. et al. Slot-die coating of perovskite solar cells: an overview. *Materials Today Communications* **22**, 100808, doi: 10.1016/j.mtcomm.2019.100808 (2020).

101. Di Giacomo, F. et al. Upscaling inverted perovskite solar cells: optimization of laser scribing for highly efficient mini-modules. *Micromachines* **11**, 1127 (2020).

102. Zhang, M. et al. High-performance photodiode-type photodetectors based on polycrystalline formamidinium lead iodide perovskite thin films. *Scientific Reports* **8**, 11157 (2018).

103. Sulaman, M. et al. Interlayer of PMMA doped with au nanoparticles for high-performance tandem photodetectors: a solution to suppress dark current and maintain high photocurrent. *ACS Applied Materials & Interfaces* **12**, 26153-26160 (2020).

104. Le, T. S. et al. Tailoring wetting properties of organic hole‐transport interlayers for slot‐die‐coated perovskite solar modules. *Solar RRL* **8**, 2400437, doi: 10.1002/solr.202400437 (2024).